

Strongly frustrated 2D magnetism in a 3D hexagonal perovskite

Bocheng Yu,^{1,*} Otkur Omar,^{2,*} Songtai Lv,^{1,*} Long Ma,³ Zhengcai Xia,⁴ Jing Meng,¹ Yanran Yang,¹ Jie Ma,⁵ Yang Xu,^{1,6} Qingfeng Zhan,^{1,6} Vladimir Yu. Pomjakushin,⁷ Haiyuan Zou,^{1,6} Shang Gao,^{2,8,†} Toni Shiroka,^{7,9,‡} and Tian Shang^{1,6,§}

¹School of Physics, East China Normal University, Shanghai 200241, China

²Department of Physics, University of Science and Technology of China, Hefei, 230026 Anhui, China

³Anhui Province Key Laboratory of Condensed Matter Physics at Extreme Conditions, High Magnetic Field Laboratory, Chinese Academy of Sciences, Hefei 230031, China

⁴Wuhan National High Magnetic Field Center and School of Physics, Huazhong University of Science and Technology, Wuhan 430070, China

⁵School of Physics and Astronomy, Shanghai Jiao Tong University, Shanghai 200240, China

⁶Key Laboratory of Polar Materials and Devices (MOE), East China Normal University, Shanghai 200241, China

⁷PSI Center for Neutron and Muon Sciences CNM, CH-5232 Villigen PSI, Switzerland

⁸Key Laboratory of Strongly-Coupled Quantum Matter Physics, Chinese Academy of Sciences, School of Physical Sciences,

University of Science and Technology of China, Hefei, Anhui 230026, China

⁹Laboratorium für Festkörperphysik, ETH Zürich, CH-8093 Zürich, Switzerland

Exotic quantum phenomena are often found to occur in spin systems that exhibit low-dimensional magnetism. By combining nuclear magnetic resonance, neutron scattering, and muon-spin spectroscopy (μ SR) techniques, we report a rare instance of strongly frustrated two-dimensional (2D) magnetism in a three-dimensional (3D) hexagonal perovskite. Here, $\text{Ba}_2\text{La}_2\text{MnTe}_2\text{O}_{12}$, a triangular-lattice magnet, is shown to undergo a magnetic transition at $T_N \approx 4.4$ K, below which the manganese moments form a 120° AFM order within the ab -plane, while staying disordered along the c -axis. This exotic ground state, which exhibits ideal 2D magnetism, is highly consistent with the persistently strong spin fluctuations and the large internal field distributions revealed by zero-field μ SR. Further, the 2D magnetism also leads to a significant frustration, much larger than that of most known magnetically-ordered frustrated systems. Our work on $\text{Ba}_2\text{La}_2\text{MnTe}_2\text{O}_{12}$ not only challenges the interpretations of magnetic order in other 3D hexagonal perovskites, but it also provides insight into how the dimensionality affects the exotic magnetic states.

I. INTRODUCTION

Low-dimensional spin systems with magnetic frustration are ideal platforms for realizing exotic quantum states, such as quantum spin liquids [1–4], spin ice [5, 6], spin super-solids [7–9], Bose-Einstein condensation [10–12], etc. Most of these low-dimensional systems host magnetic lattices with geometric frustration (also known as magnetic frustration), including kagome and triangular lattices [13–25]. The latter systems are among the best models for studying the occurrence of exotic quantum states [13–20].

To the triangular lattice magnets belong also the hexagonal perovskites $A_4BB'_2\text{O}_{12}$ [see Figs. 1(a) and (b)], with $A = \text{Sr}, \text{Ba}, \text{La}$; $B = \text{Co}, \text{Ni}, \text{Mn}$; and $B' = \text{Re}, \text{W}, \text{Te}$ [26–31]. Depending on the stoichiometry of the B' site, the A site may be occupied entirely by Ba^{2+} , Sr^{2+} , or La^{3+} ions, or by a combination of them [29]. In this structure, the BO_6 octahedra share their corners with the $B'\text{O}_6$ octahedra via oxygen atoms, which leads to two types of superexchange interaction paths, i.e., ferromagnetic (FM) $B\text{--O--B'--O--B}$ and antiferromagnetic (AFM) $B\text{--O--O--B}$ [see Fig. 1(c)] [29]. The competition between these FM and AFM interactions eventually determines the magnetic ground state of $A_4BB'_2\text{O}_{12}$, which can be tuned by physical pressure or by chemical substitutions (see Table S1 in the Supplementary Materials [32] and also Refs. 33–36 therein). For example, $\text{Ba}_2\text{La}_2\text{NiTe}_2\text{O}_{12}$ shows an AFM ground state below $T_N \approx 10$ K [28], while

$\text{Ba}_2\text{La}_2\text{NiW}_2\text{O}_{12}$ is ferromagnetically ordered below $T_C \approx 6.3$ K [27]. Moreover, field-induced up-up-down (UUD) states and magnetization plateaus have been observed in the spin-1/2 or spin-1 triangular-lattice antiferromagnets $\text{Ba}_2\text{La}_2B\text{Te}_2\text{O}_{12}$ ($B = \text{Co}, \text{Ni}$) [26, 28].

Since the $\text{Ba}_2\text{La}_2BB'_2\text{O}_{12}$ family of materials exhibits rich quantum magnetic properties [26–31], it is of interest to investigate its last member, namely, $\text{Ba}_2\text{La}_2\text{MnTe}_2\text{O}_{12}$ (BLMTO) which, to the best of our knowledge, has not yet been synthesized or studied. In this paper, we report the successful synthesis of BLMTO and the systematic study of its magnetic properties by combining nuclear magnetic resonance (NMR), neutron scattering, and muon-spin spectroscopy (μ SR) techniques. The ground state of the triangular-lattice XXZ model (TL- XXZ) was constructed with the tensor network approach to capture the magnetic properties of BLMTO. Our key observation, the presence of strongly frustrated two-dimensional (2D) magnetism in three-dimensional (3D) materials with a magnetic triangular lattice, suggests that BLMTO and related compounds represent a remarkable platform to study the dimensionality effects on the exotic magnetic states. The hallmark of ideal 2D magnetism within the ab -plane of BLMTO — the suppression of long-range order — is manifested here through the magnetic disorder along the c -axis.

II. EXPERIMENTAL DETAILS

A polycrystalline sample of BLMTO was first synthesized by solid-state reaction methods. Stoichiometric amounts of BaCO_3 (99.99%), La_2O_3 (99.99%), MnCO_3 (99.99%), and TeO_2 (99.999%) were mixed and ground thoroughly for 2 h. The mixture was placed into an alumina crucible and sintered at 1050°C for 24 h. After grinding the samples

* These authors contributed equally.

† Corresponding author: sgao@ustc.edu.cn

‡ Corresponding authors: tshiroka@phys.ethz.ch

§ Corresponding authors: tshang@phy.ecnu.edu.cn

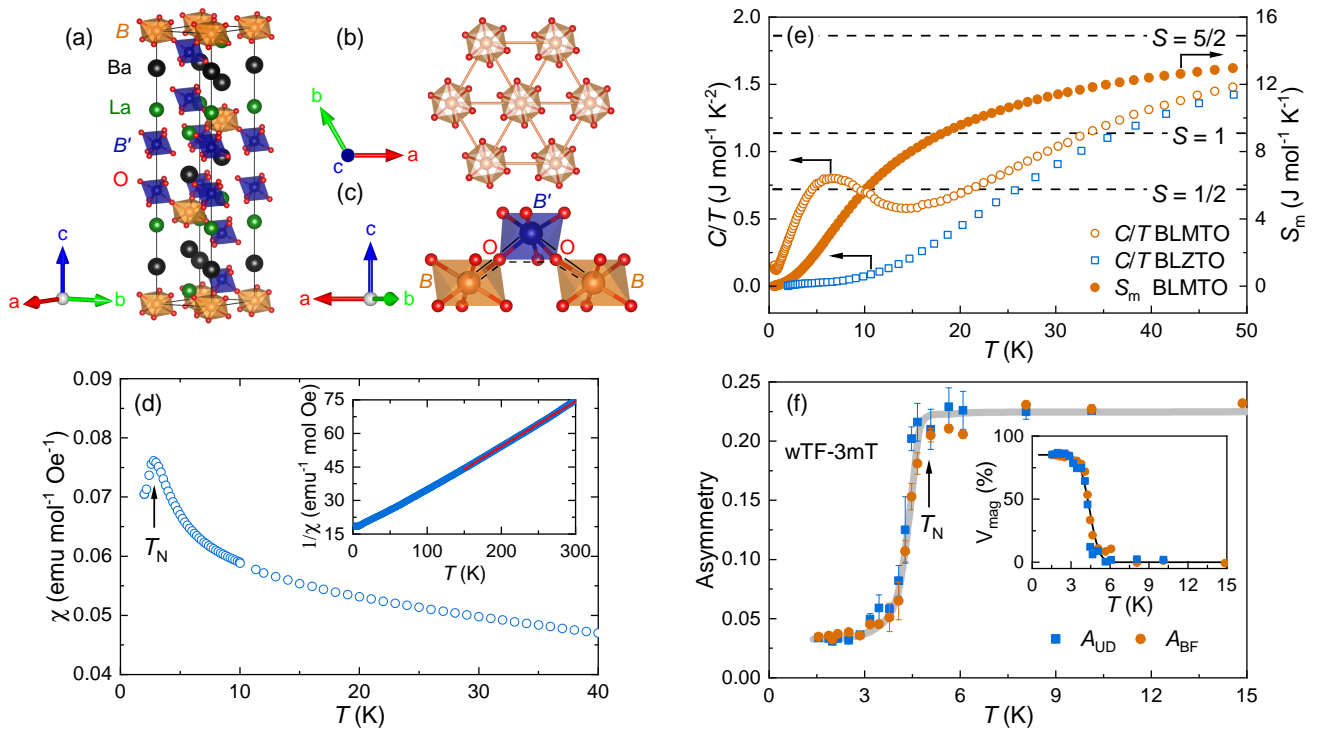


FIG. 1. (a) Crystal structure of $\text{Ba}_2\text{La}_2\text{BB}'_2\text{O}_{12}$ ($B = \text{Co, Ni, Mn}$; $B' = \text{W, Te, Re}$). (b) Triangular sublattice of the magnetic B ions. (c) Pathways of the $B\text{-O-B}'\text{-O-B}$ (black solid lines) and $B\text{-O-O-B}$ (black dashed lines) superexchange interactions. (d) Temperature-dependent magnetic susceptibility $\chi(T)$ for BLMTO collected in a field of 50 mT. The inset shows the inverse susceptibility $1/\chi(T)$. The red solid line represents a fit to the Curie-Weiss law. (e) Temperature-dependent specific heat $C(T)/T$ (left-axis) and magnetic entropy $S_m(T)$ (right-axis) of BLMTO. The magnetic specific heat was obtained by subtracting the specific heat of the nonmagnetic $\text{Ba}_2\text{La}_2\text{ZnTe}_2\text{O}_{12}$ (BLZTO) (empty circles and squares, resp., see details in Fig. S4 [32]) from the raw data. Dashed lines mark the entropy values $R \ln(2S + 1)$, with $S = 1/2, 1,$ and $5/2$, respectively. (f) Temperature dependence of nonmagnetic asymmetry A_{NM} of wTF- μ SR spectra for BLMTO, obtained in a 3-mT transverse field. Data from the up-down (UD) and backward-forward (BF) detectors are highly consistent. The inset shows the magnetic volume fraction vs temperature. The solid line is a fit to the phenomenological relation $V_{\text{mag}}(T) = V_{\text{mag}}(0) \frac{1}{2} [1 - \text{erf}(\frac{T-T_N}{\sqrt{2}\Delta T})]$, where ΔT , $V_{\text{mag}}(0)$ and $\text{erf}(T)$ are the transition width, the zero-temperature magnetic volume, and the error function, respectively.

again, the powders were pressed into pellets and sintered at 1050°C for extra 24 h. Heat-capacity and magnetization measurements were performed on a Quantum Design physical property measurement system and magnetic property measurement system, respectively. The high-field magnetization was measured using an induction method with a multilayer pulse magnet at the Wuhan National Pulsed High Magnetic Field Center and a home-built vibrating sample magnetometer at the Anhui Key Laboratory of Low-Energy Quantum Materials and Devices. To capture the magnetic properties of the BLMTO powder, the ground state of the TL- XXZ model was constructed using the tensor network approach based on the projected entangled simplex state (PESS) ansatz in the thermodynamic limit [37]. The NMR measurements were performed on ^{139}La nuclei ($\gamma_n = 6.014\text{ MHz/T}$, $I = 7/2$). The frequency-swept spectrum was obtained by integrating the spectral weight at different frequencies. The spin-lattice relaxation rate was measured by the inversion-recovery method, and evaluated by fitting the time-dependent nuclear magnetization to the standard relaxation function for $I = 7/2$. High-resolution neutron powder diffraction (NPD) measurements were carried out on the HRPT powder diffractometer at the Swiss Spallation Neutron Source (SINQ) of the Paul Scherrer Institut (PSI) in Switzerland [38]. The μ SR measurements were carried out at the general-purpose surface-muon (GPS) instrument at the πM3 beam line of the Swiss muon source (S μ S) at PSI in Villigen, Switzerland. For the μ SR measurements, a $\sim 1\text{-mm}$ thick pellet with a

diameter of $\sim 8\text{ mm}$ was positioned on a copper plate using diluted GE varnish, which ensures thermalization at low temperatures. All the μ SR spectra were collected upon heating the sample and were analyzed by means of the musrfit software package [39]. All the measurements reported in this paper were performed on the same batch of BLMTO polycrystalline samples.

III. RESULTS AND DISCUSSION

The crystal structure of BLMTO was checked by NPD measurements. Refinements of the NPD patterns confirmed the hexagonal structure of BLMTO [Fig. 1(a)] with a space group $R\bar{3}$ (No. 148) (see Fig. S1 and Table S2 in the Supplementary Materials) [32]. A tiny amount of extra La_2TeO_6 (3.45%) and $\text{Ba}_{1/3}\text{La}_{2/3}\text{MnO}_3$ (0.36%) spurious phases were identified, the former was also detected by x-ray diffraction (see Fig. S2 [32]). In addition, the cations at the A and B/B' sites are well ordered in BLMTO, with no detectable antisite disorder. As shown in Fig. 1(d), the temperature-dependent magnetic susceptibility $\chi(T)$ exhibits a distinct peak at $T_N = 3\text{ K}$, corresponding to an AFM transition in BLMTO. The inset shows the inverse susceptibility versus temperature, where the solid red line is a fit to the Curie-Weiss law, which yields an effective moment $\mu_{\text{eff}} = 6.2(2)\ \mu_B$ and a Curie-Weiss temperature $\theta_{\text{CW}} = -62.4(5)\text{ K}$. The negative θ_{CW} indicates the presence of dominant AFM interactions in BLMTO, while

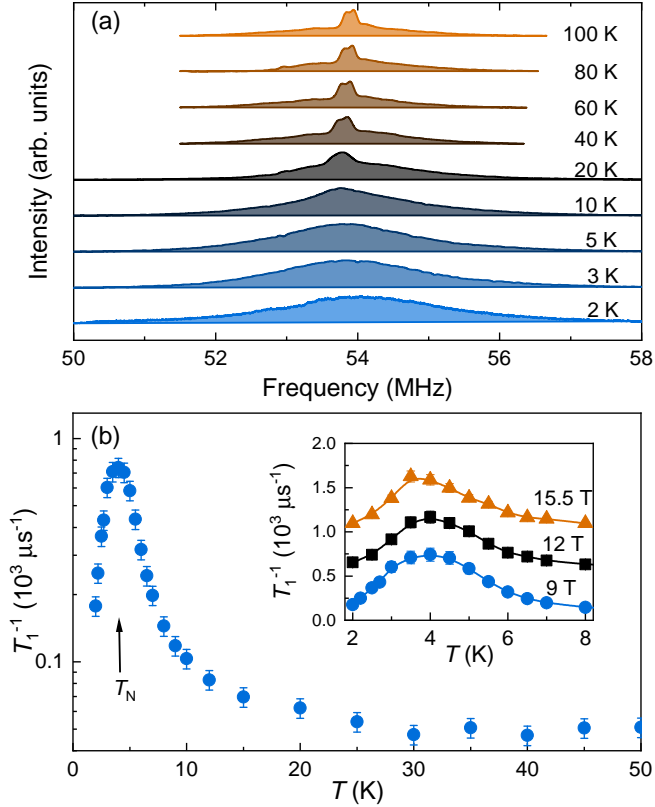


FIG. 2. (a) ^{139}La -NMR spectra of BLMT0 collected at different temperatures in an applied magnetic field of 9 T. The NMR spectra in other fields show similar features. (b) Spin-lattice relaxation rates T_1^{-1} of BLMT0 vs temperature, measured at 9 T. The inset highlights the mostly unchanged T_1^{-1} peak with the magnetic field. For clarity, the T_1^{-1} values are shifted vertically.

the effective moment suggests a high spin state of Mn^{2+} ions ($S = 5/2$, $\mu_{\text{eff}} = 5.9 \mu_B$). Similar results were obtained for the $\chi(T)$ data collected under various magnetic field up to 7 T (see Fig. S3 [32]). As shown in Fig. 1(e), the zero-field specific heat $C(T)/T$ of BLMT0 exhibits a broad hump at $T \sim 6$ K. Such a hump-like anomaly is robust against external magnetic fields (Fig. S4 [32]) and is clearly distinct from the typical λ -type transition in magnetic materials with a long-range order [26, 27, 29]. The magnetic entropy S_m extends to 50 K, which is almost 10 times higher than the magnetic ordering temperature of BLMT0. S_m reaches $13.1 \text{ J mol}^{-1} \text{ K}^{-1}$ at 50 K, accounting for 88% of the theoretical value for a $S = 5/2$ system. These features differ clearly from those of the isostructural $(\text{Sr,Ba})_2\text{La}_2\text{NiW}_2\text{O}_{12}$ and $\text{Ba}_2\text{La}_2\text{CoTe}_2\text{O}_{12}$ [26, 27, 29] and reflect the strong magnetic frustrations in BLMT0 (see details below).

The magnetic transition temperature was also determined using weak transverse-field (wTF)- μSR measurements. In this case, a field of 3 mT was applied perpendicular to the initial muon-spin direction. In the paramagnetic (PM) state, this field leads to oscillations (see Fig. S5 [32]). In the long-range ordered AFM state, the same 3-mT field is much smaller than the internal fields (see below). Consequently, upon entering the AFM state, the muon spins precess at frequencies reflecting the internal fields at the muon-stopping sites rather than the weak applied field. Consequently, the PM or nonmagnetic (NM) sample fraction can be determined from the oscillation amplitude of wTF- μSR . The asymmetry values A_{NM} of wTF- μSR spectra shown in Fig. 1(f) start to

decrease near the onset of AFM order. The temperature evolution of the magnetic volume fraction can be derived from $V_{\text{mag}}(T) = 1 - A_{\text{NM}}(T)/A_{\text{NM}}(T > T_N)$. The $V_{\text{mag}}(T)$ values for BLMT0 are summarized in the inset of Fig. 1(f), where we show the AFM ordering temperature $T_N = 4.4(2)$ K, the transition width $\Delta T = 0.6(1)$ K, and the zero-temperature magnetic volume fraction $V_{\text{mag}}(0) = 85(1)\%$. The slightly reduced magnetic volume fraction is due to either the presence of spurious phases (see Figs. S1 and S2 [32]), or to muons stopping on the copper sample holder. The latter usually results in a temperature-independent μSR asymmetry. The sharp AFM transition indicates that the broad hump in the specific heat is indeed related to magnetic frustration, rather than to the polycrystalline nature of BLMT0.

Figure 2(a) shows the ^{139}La -NMR spectra of BLMT0 collected at various temperatures in an applied magnetic field of 9 T. In the high temperature range (i.e., $T \geq 40$ K), the ^{139}La -NMR spectra consist of a split central peak, attributed to the transition between the $+1/2$ and $-1/2$ nuclear spin states, and a broad featureless background. The simulation of the 100-K NMR spectrum (see Fig. S6 [32]) provides a quadrupole resonance frequency $\nu_Q \approx 1.6$ MHz. The line splitting of the central peak is attributed to the second-order correction to the central frequency of the quadrupole interaction. The background signal arises mainly from the satellite lines of crystals whose c -axes are perpendicular to the external field. The absence of singularities in the background signal suggests a broad distribution of local electric-field gradients, which could be caused by disorder effects or local lattice distortions.

Upon lowering the temperature below 40 K, the split peak develops into a single broad peak which, below 20 K, is barely visible, as it merges with the very broad background contributed by the satellites. The significant broadening we observe most likely reflects the formation of the short-range order in BLMT0. At high temperatures, the spin-lattice relaxation rate T_1^{-1} is almost temperature independent (see Fig. S7 [32]). It starts to increase below ~ 25 K, to drop again at $T < T_N$ [see Fig. 2(b)]. T_1^{-1} measures the weighted sum of the dynamical spin susceptibility at the NMR frequency over the first Brillouin zone, which provides clear signatures of evolving spin correlations. Hence, an increase in T_1^{-1} reflects the enhanced low-energy spin fluctuations as one approaches the magnetic order. Although T_N shifts slightly with field (to 3.5 K at 15.5 T – see inset), the temperature dependence of $T_1^{-1}(T)$ is quite robust against the external magnetic field.

To further investigate the local magnetic properties of BLMT0, a series of zero-field (ZF)- μSR spectra were collected at different temperatures, covering both the PM and AFM states. As shown in Fig. 3(a), ZF- μSR spectra in the AFM state (e.g., at 1.5 K) are characterized by highly damped oscillations, typical of long-range magnetic order, superimposed on a slowly decaying relaxation, observable only at long times. While, in the PM state, ZF- μSR spectra still exhibit a relatively fast muon-spin depolarization (e.g., $\sim 2 \mu\text{s}^{-1}$ at 10 K), implying the presence of strong spin fluctuations. In the AFM state, ZF- μSR spectra of BLMT0 were modeled using the equation:

$$A_{\text{ZF}}(t) = A_1 \left[\frac{2}{3} \cos(\omega t + \phi) e^{-\lambda_{\text{r}} t} + \frac{1}{3} e^{-\lambda_{\text{l}} t} \right] + A_2 e^{-\lambda_{\text{tail}} t} + A_{\text{bg}}. \quad (1)$$

Here, A_1 and A_2 represent the asymmetries of the two

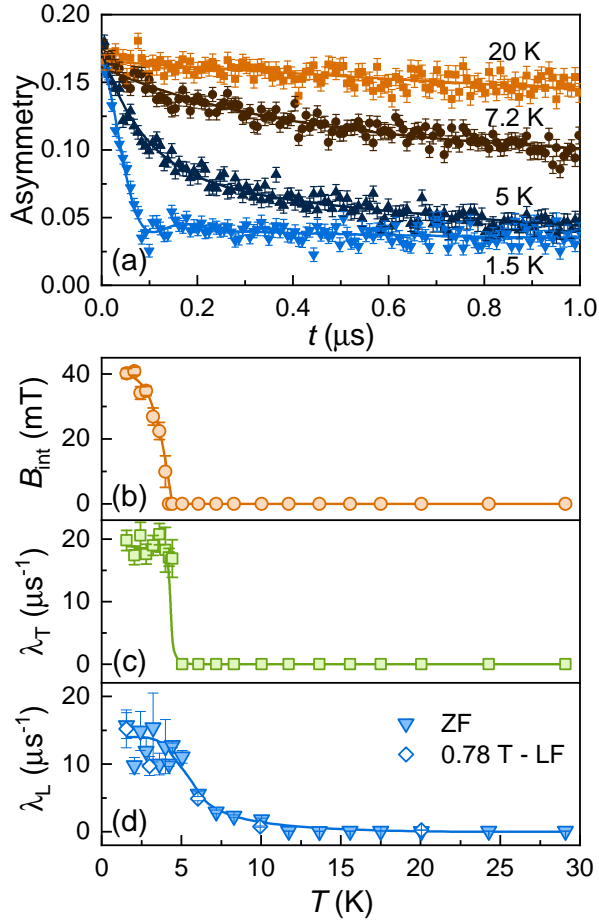


FIG. 3. (a) ZF- μ SR spectra of BLMTO collected at representative temperatures. The full-time scale spectra are shown in Fig. S8, while the decomposed components are presented in Fig. S9 [32]. Solid lines are fits to Eq. (1) and Eq. (2) for the AFM and PM states, respectively. Temperature-dependent internal field $B_{\text{int}}(T)$ (b), transverse muon-spin relaxation rate $\lambda_T(T)$ (c), and longitudinal muon-spin relaxation rate $\lambda_L(T)$ (d). The λ_L values from μ SR spectra in a longitudinal field of 0.78 T are also shown in panel (d). Note that λ_L is two orders of magnitude larger than λ_{tail} (see Fig. S9 [32], where also the asymmetries are summarized). The solid lines in panels (b)–(d) are guides to the eyes.

nonequivalent muon-stopping sites; A_{bg} represents the background asymmetry, accounting for the muons stopped in the copper sample holder or in the spurious phases. A_{bg} was determined to be ~ 0.02 and was fixed when analyzing the ZF- μ SR spectra. This background signal corresponds to approximately 11% of the total asymmetry A_{ZF} , and is highly consistent with the nonmagnetic volume fraction ($\sim 15\%$) determined from the wTF- μ SR [see Fig. 1(f)]. $\omega (= \gamma_{\mu} B_{\text{int}})$ is the muon-spin precession frequency, with $\gamma_{\mu} = 2\pi \times 135.5 \text{ MHz/T}$ the muon gyromagnetic ratio and B_{int} the local field sensed by muon spins; ϕ is the initial phase; λ_T and λ_L are the transverse and longitudinal muon-spin relaxation rates. In BLMTO, muons stopping at the second site (here, second addend) do not undergo any precession, but show only a slow relaxation, here described by λ_{tail} . In the PM state, the ZF- μ SR spectra were modeled using the equation:

$$A_{\text{ZF}}(t) = A_1 e^{-\lambda_L t} + A_2 e^{-\lambda_{\text{tail}} t} + A_{\text{bg}}, \quad (2)$$

with all the parameters being identical to those in Eq. (1).

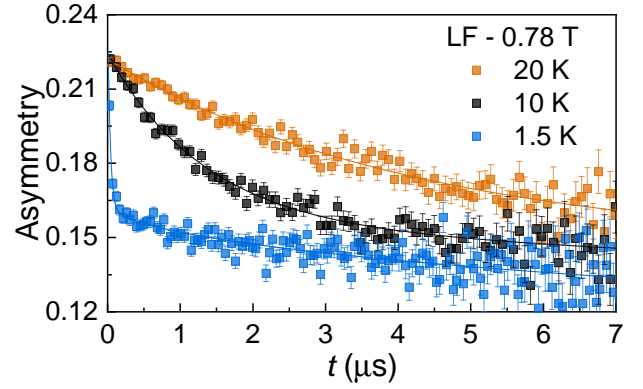


FIG. 4. LF- μ SR spectra collected in a magnetic field of 0.78 T at selected temperatures, covering both the AFM and PM states of BLMTO. Solid lines are fits to Eq. (2). The applied magnetic field is parallel to the muon-spin direction. The LF- μ SR spectra collected at $T = 60 \text{ K}$ in different magnetic fields are shown in Fig. S10 [32].

Internal local field B_{int} increases monotonically as the temperature decreases below T_N , reaching $\sim 40 \text{ mT}$ at 1.5 K [Fig. 3(b)]. Such field is almost 10 times smaller than that observed in the isostructural $\text{Ba}_2\text{La}_2\text{NiW}_2\text{O}_{12}$, the latter showing an FM ground state below 6 K [27]. λ_T is a measure of the width of the static magnetic field distribution at the muon-stopping site, but it is also affected by dynamic effects, as e.g., spin fluctuations. Conversely, λ_L is determined solely by spin fluctuations. In BLMTO, λ_T is zero in the PM state, but it becomes increasingly prominent and temperature independent at $T < T_N$ [Fig. 3(c)]. Such a large λ_T at temperatures far below T_N is unusual for an antiferromagnet, and implies a disordered field distribution in the AFM state of BLMTO. At $T = 1.5 \text{ K}$, λ_T is about $\sim 20 \mu\text{s}^{-1}$ in BLMTO, which is almost 4 times larger than in $\text{Ba}_2\text{La}_2\text{NiW}_2\text{O}_{12}$ [27]. Such a significantly inhomogeneous field distribution in the AFM state of BLMTO is most likely attributed to its disordered magnetic structure along the c -axis (see details below). For typical materials with a long-range (anti)ferromagnetic order [27, 40, 41], λ_L diverges near T_N , followed by a significant drop at $T < T_N$, indicating that spin fluctuations are the strongest close to the onset of the magnetic order. In contrast, in BLMTO, λ_L increases continuously as the temperature decreases below 12 K [Fig. 3(d)], where also the specific heat shows an upturn [Fig. 1(e)] thus indicating enhanced spin fluctuations at low temperatures. At base temperature, λ_L reaches $\sim 16 \mu\text{s}^{-1}$, i.e., a comparable value to λ_T [Fig. 3(c)]. Such strong spin fluctuations in the AFM state are quite robust against the external field. Figure 4 shows the longitudinal-field (LF-) μ SR spectra collected in a magnetic field of 0.78 T at temperatures covering both the AFM and PM states of BLMTO. At $T = 1.5 \text{ K}$, the internal field of 40 mT is significantly smaller than the external longitudinal field of 0.78 T. As a consequence, muon spins do not precess around the local field. In this case, the LF- μ SR spectra can also be modeled using Eq. (2). The derived muon-spin relaxation rates λ_L and λ_{tail} are summarized in Fig. 3(d) and Fig. S11 [32], respectively. The λ_L values in a 0.78-T field almost overlap with the zero-field values. Such robust spin fluctuations are attributed to the disordered magnetic structure along the c -axis and the strong magnetic frustration of the Mn^{2+} triangular lattice. By contrast, the

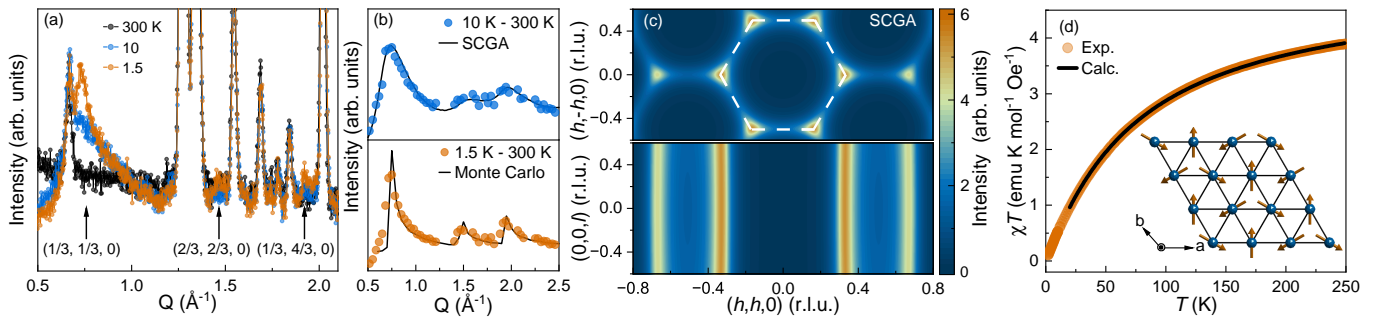


FIG. 5. (a) NPD patterns collected at $T = 1.5, 10,$ and 300 K reveal asymmetric magnetic Bragg peaks with $\mathbf{q} = (1/3, 1/3, 0), (2/3, 2/3, 0),$ and $(1/3, 4/3, 0)$ (marked by arrows). (b) Comparison of experimental- and simulated NPD spectra. Upper panel: experimental data at 10 K is fitted using the J_1 - J_2 - J_c model through the SCGA method. Lower panel: experimental data at 1.5 K and the simulated pattern calculated using the fitted J_1 - J_2 - J_c model through classical Monte Carlo simulations. (c) Simulated diffuse neutron scattering patterns in the $(h, k, 0)$ and (h, h, l) planes using the fitted J_1 - J_2 - J_c calculated from the SCGA method at 10 K. (d) Temperature dependence of the reduced magnetic susceptibility χT of BLMTO, measured at 7 T. The solid line represents the theoretical calculation using the SCGA method. The inset depicts the 120° AFM correlations among the Mn^{2+} electronic moments in the ab -plane.

weak relaxation (i.e., λ_{tail}) is suppressed by the longitudinal field (see Fig. S11 [32]). Note that, the decrease of T_1 at $T < T_N$ in Fig. 2(b) indicates a slowing down of spin fluctuations in the AFM state, which appears to contradict λ_L in Fig. 3(d). However, NMR and μSR measurements were performed under very different magnetic-field conditions: the former in fields of $9, 12,$ and 15.5 T and the latter in fields of 0 and 0.78 T. Although muon-spin relaxation is robust against longitudinal fields up to 0.78 T, it can be suppressed at larger magnetic fields, where the spin fluctuations may also be suppressed. Further μSR investigations are required to clarify this behavior as a function of the applied field.

Neutron scattering measurements were employed to reveal the magnetic structure of BLMTO. As shown in Fig. 5(a), NPD patterns exhibit a distinct broad hump near $\mathbf{q} = (1/3, 1/3, 0)$ as the temperature approaches 10 K. Such a hump reflects the emergence of short-range order already above T_N , leading to a highly asymmetric magnetic peak at $Q \sim 0.75 \text{ \AA}^{-1}$ at 1.5 K. The asymmetric magnetic peak suggests the presence of two-dimensional magnetic correlations in BLMTO [42]. To quantitatively analyze the spin correlations, we employ complementary theoretical approaches in the different temperature regimes. Above T_N (10 K), the self-consistent Gaussian approximation (SCGA) method [43] successfully models the diffuse scattering [Fig. 5(b), upper panel] and the temperature dependence of the reduced magnetic susceptibility, χT [Fig. 5(d)], using an antiferromagnetic triangular-lattice model (AFTL) with a fitted coupling strength of $J_1 = 0.323(6)$, $J_2 = 0.028(1)$, and $J_c = -0.007(4)$ meV. Here, $J_1, J_2,$ and J_c represent the nearest-neighbor, next-nearest-neighbor coupling in the ab -plane, and the interlayer coupling, respectively. Notably, an almost zero J_c value confirms the 2D character of BLMTO. Below T_N (1.5 K), classical Monte Carlo simulations were utilized to capture the quasi-long-range order within the triangular layers. As shown in the lower panel of Fig. 5(b), the asymmetric peaks centered around $\mathbf{q} = (1/3, 1/3, 0), (2/3, 2/3, 0),$ and $(1/3, 4/3, 0)$ are well reproduced by the fitted AFTL model. As shown in Fig. 5(c), diffuse scattering calculated using the SCGA method at 10 K suggest that the scattering intensity is centered around the K - $(1/3, 1/3, l)$ points regardless of the l value. This key fact reveals two-dimensional spin fluctuations that form a typical 120° order in the ab -plane, but remain disordered along the c -axis,

as has been previously observed in other triangular-lattice compounds [44–47].

Previous neutron studies of the isostructural $\text{Ba}_2\text{La}_2\text{B-Te}_2\text{O}_{12}$ ($B = \text{Co}, \text{Ni}$) compounds have proposed magnetic structures based solely on background-subtracted diffraction patterns, without a detailed analysis [26, 28, 31]. In particular, the nearly degenerate $(1/3, 1/3, 0)$ and $(1/3, 1/3, 1)$ magnetic peaks in these materials can hardly distinguish between 3D ordered states and 2D magnetism. By combining the SCGA method with Monte-Carlo simulations, we establish an exotic magnetic ground state that is better in accord with the materials' dimensional constraints, namely, 120° AFM order within the ab -plane, but magnetic disorder along the c -axis. Such a unique magnetic order reflects a quasi-static magnetic ground state of BLMTO, which is consistent with the persistent muon-spin relaxation rate in its AFM state [see Fig. 3(d)]. The revised 2D-like magnetic structure not only challenges the interpretation of 3D-ordered states in $A_4\text{BB}'_2\text{O}_{12}$ family of materials, but it also provides further insight into how the dimensionality affects the exotic magnetic states.

IV DISCUSSION

The triangular lattice usually promotes a large magnetic frustration [13–20, 48–51], often quantified by the ratio $f = |\theta_{\text{CW}}|/T_N$, with θ_{CW} the Curie-Weiss temperature, as estimated from the temperature-dependent magnetic susceptibility. For BLMTO, the $f = 14.2$ exceeds the threshold value ($f = 10$) for strongly frustrated magnets, and is much larger than that of other frustrated magnets with a long-range order (see Table I). Such a significant magnetic frustration leads to persistent spin fluctuations in the magnetically ordered state of BLMTO, reflected in continuously increasing of muon-spin relaxation rates [Fig. 3(d)]. Indeed, λ_L of BLMTO is almost 10 times larger than that of most QSL candidates. In addition to the easy-axis anisotropy, such fluctuations may also lead to a $1/3$ -saturation-magnetization ($M_s/3$) plateau in many frustrated magnets, corresponding to an intermediate UUD phase [14, 16, 26, 28, 52, 53].

To investigate the effects of magnetic fluctuations, the field-dependent magnetization $M(H)$ of BLMTO was measured at 1.8 K in magnetic fields up to 49 T. As shown in

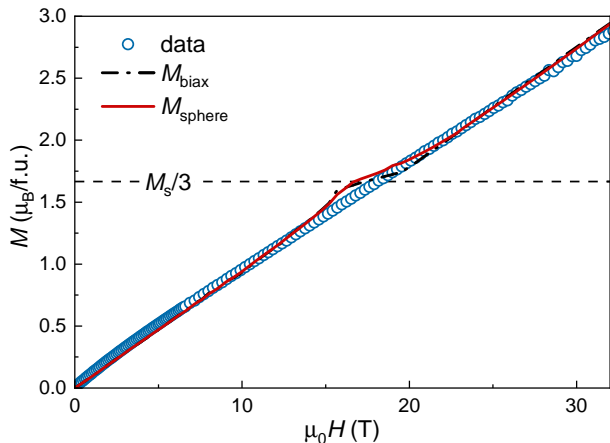


FIG. 6. Field-dependent magnetization $M(H)$ collected at $T = 1.8$ K in magnetic fields up to 32 T (data up to 49 T are presented in Fig. S12 [32]). Red solid and black dash-dotted lines represent the calculated magnetization using spherical (M_{sphere}) and weighted-biaxial averages (M_{biax}), respectively. The dashed horizontal line denotes the $M_s/3$ magnetization plateau.

Table I. Magnetic frustration ratio f and ZF muon-spin relaxation rates λ_L at base temperature for various types of magnets.

Compound	Magnetic lattice	f	λ_L (μs^{-1})	Ref.
ZnCu ₃ (OH) ₆ Cl ₂	Kagome	∞	0.5	[22, 23]
Tm ₃ Sb ₃ Zn ₂ O ₁₄	Kagome	∞	1.3	[21]
MgFe ₃ (OH) ₆ Cl ₂	Kagome	3.9	0.08	[54]
H ₃ LiIr ₂ O ₆	Honeycomb	∞	4.3	[55]
Na ₂ IrO ₃	Honeycomb	8.3	10	[24]
α -RuCl ₃	Honeycomb	2.9	3.5	[56, 57]
YbMgGaO ₄	Triangular	∞	0.3	[58]
NaYbO ₂	Triangular	∞	0.9	[19, 59]
Ba ₂ La ₂ NiW ₂ O ₁₂	Triangular	4.1	0.53	[27]
Ba ₂ La ₂ MnTe ₂ O ₁₂	Triangular	14.2	16	This work

Fig. 6, the magnetization is almost linear in field, confirming the absence of magnetization plateaus and UUD phases in BLMTMO. Since both J_2 and J_c are much weaker than J_1 , we employ the nearest-neighbor (NN) TL-XXZ model to calculate the magnetization of BLMTMO. This model is described by the Hamiltonian:

$$\mathcal{H} = J \sum_{\langle i,j \rangle} (S_i^x S_j^x + S_i^y S_j^y + \eta S_i^z S_j^z) - h_x \sum_i S_i^x - h_z \sum_i S_i^z. \quad (3)$$

Here, $J > 0$ is the AFM exchange coupling, $S_i^{x,y,z}$ are the spin operators at the i -th site of the triangular lattice; $\langle i, j \rangle$ denotes the NN pairs; $\eta (< 1)$ suggests an easy-plane anisotropy; h_x and h_z represent the reduced magnetic fields within the ab -plane or along the c -axis, respectively. The ground state wave function of the system is obtained using the PESS method (Fig. S13 and Note S1 [32]). After convergence, the expectation values of the spin operator are calculated to determine the magnetization M_x and M_z induced by the fields h_x and h_z , respectively. Assuming the susceptibility can be decomposed into constant components along both the x - and z -directions, the magnetization of powder samples can be evaluated using a biaxial average, namely, $M_{\text{biax}} = (2M_x + M_z)/3$. As shown by the black dash-dotted line in Fig. 6, by using the J ($= J_1$) value determined from NPD (see Fig. 5) and assuming $\eta = 0.9$, the calculated M_{biax} agrees reasonably well with the experimental

data. However, M_{biax} exhibits a slight bump around $M_s/3$, here attributed to the stabilization of a UUD phase by h_x for a wide range of η -s (see Fig. S14 and Note S2 [32]). This indicates that the NN TL-XXZ model serves only as an approximate effective model for BLMTMO. The complete vanishing of the plateau requires taking into account additional, more complex interactions, which would greatly increase the computational complexity of the tensor network approach. Nevertheless, the NN TL-XXZ model is a good base for further improvements. For polycrystalline (powder) materials, the applied magnetic field acts only as an average effect, leading to a rather coarse biaxial averaging of the magnetization. Therefore, we further performed a spherical averaging (see Fig. S15 and Note S2 [32]), obtaining a weaker magnetization bump around $M_s/3$ (Fig. 6).

The above discrepancy can be understood by considering the following factors. In general, the width of the $M_s/3$ magnetization plateau is determined by both the magnetic exchange coupling and the effective spin, namely, $\Delta H = 1.8J/2S$ [52, 60]. For Mn^{2+} ($S = 5/2$), its relatively large effective spin renders the $M_s/3$ plateau less distinct compared to Co^{2+} ($S = 1/2$) and Ni^{2+} ($S = 1$) ions with small effective spin [26, 28]. Different from the easy-axis anisotropy, that generally stabilizes the UUD phase, significant quantum fluctuations are needed to maintain such phase in easy-plane anisotropy compounds [8, 9, 60], such as BLMTMO. In addition, in the XXZ model, other magnetic interactions beyond NN might need to be considered. For example, the next-nearest-neighbor (NNN) interaction favors the stripe phase over the UUD phase in a Heisenberg antiferromagnet on a frustrated triangular lattice [61]. Such a NNN interaction can also result in a less distinguishable $M_s/3$ plateau [62, 63], resembling the results of BLMTMO (see Fig. 6). Although the estimated $J_2 = 0.028$ meV is much smaller than that of $J_1 = 0.323$ meV, its presence might affect the magnetization plateau in BLMTMO. Given that the NNN interaction significantly increases the degrees of freedom of the minimum unit to describe the whole lattice system, alternative approaches, such as spin-wave theory, may provide further insights.

V. CONCLUSION

In summary, a new member of the hexagonal perovskites $A_4BB_2'O_{12}$ with magnetic triangular lattice, namely, $\text{Ba}_2\text{La}_2\text{MnTe}_2\text{O}_{12}$, was synthesized, and its magnetic properties were systematically studied by a variety of techniques. BLMTMO undergoes a magnetic transition at $T_N \sim 4.4$ K, attributed to the AFM order of the Mn^{2+} sublattice. The NPD measurements reveal an exotic magnetic ground state in BLMTMO, where manganese moments form a 120° AFM order within the ab -plane, but are disordered along the c -axis. Such a magnetic state is highly consistent with the persistently strong spin fluctuations and large internal field distributions in the ZF- μ SR spectra even below T_N . BLMTMO represents a rare case of a 3D hexagonal perovskite hosting a strongly frustrated 2D magnetism. Such a revised 2D magnetism challenges the interpretation of the 3D ordered states in the $A_4BB_2'O_{12}$ family of materials. Though BLMTMO exhibits strong magnetic frustration and fluctuations, their effects are largely suppressed by the high-spin state of Mn^{2+} and the easy-plane anisotropy, both of which are unfavorable to a quantum phase stabilization. Future studies, including

single-crystal growth and chemical substitutions on A or B' sites, are highly desirable to search for possible quantum phase transitions in BLMTO.

ACKNOWLEDGMENTS

This work was supported by the National Natural Science Foundation of China (Grant Nos. 12374105, 12350710785, and 12561160109), and the Fundamental Research Funds for the Central Universities. H.Z. and S.L. acknowledge the support from the National Natural Science Foundation of

China via Grant No. 12274126, while J.M. was supported via Grant Nos. U2032213 and 12334008. W.W. and S.G. acknowledge financial support from the National Science Foundation of China (Grant No. 12374152). Z. X. acknowledge the support the National Key Research and Development Program of China (Grant No. 2023YFA1406500). Neutron powder diffraction and muon-spin spectroscopy measurements were performed at the Swiss spallation neutron source SINQ and Swiss muon source ($S\mu S$) of the Paul Scherrer Institut (PSI) in Switzerland. We also acknowledge the allocation of beam time at HRPT diffractometer and GPS spectrometer.

-
- [1] L. Balents, Spin liquids in frustrated magnets, *Nature* **464**, 199 (2010).
- [2] C. Broholm, R. J. Cava, S. A. Kivelson, D. G. Nocera, M. R. Norman, and T. Senthil, Quantum spin liquids, *Science* **367**, eaay0668 (2020).
- [3] Y. Zhou, K. Kanoda, and T.-K. Ng, Quantum spin liquid states, *Rev. Mod. Phys.* **89**, 025003 (2017).
- [4] L. Savary and L. Balents, Quantum spin liquids: A review, *Rep. Prog. Phys.* **80**, 016502 (2017).
- [5] S. H. Skjærø, C. H. Marrows, R. L. Stamps, and L. J. Heyderman, Advances in artificial spin ice, *Nat. Rev. Phys.* **2**, 13 (2020).
- [6] M. J. P. Gingras and P. A. McClarty, Quantum spin ice: A search for gapless quantum spin liquids in pyrochlore magnets, *Rep. Prog. Phys.* **77**, 056501 (2014).
- [7] D. Heidarian and K. Damle, Persistent supersolid phase of hard-core bosons on the triangular lattice, *Phys. Rev. Lett.* **95**, 127206 (2005).
- [8] D. Yamamoto, G. Marmorini, and I. Danshita, Erratum: Quantum phase diagram of the triangular-lattice XXZ model in a magnetic field, *Phys. Rev. Lett.* **112**, 259901 (2014).
- [9] D. Sellmann, X.-F. Zhang, and S. Eggert, Phase diagram of the antiferromagnetic XXZ model on the triangular lattice, *Phys. Rev. B* **91**, 081104 (2015).
- [10] T. Matsubara and H. Matsuda, A lattice model of liquid helium, I, *Prog. Theor. Phys.* **16**, 569 (1956).
- [11] T. Giamarchi, C. Rüegg, and O. Tchernyshyov, Bose-Einstein condensation in magnetic insulators, *Nat. Phys.* **4**, 198 (2008).
- [12] V. Zapf, M. Jaime, and C. D. Batista, Bose-Einstein condensation in quantum magnets, *Rev. Mod. Phys.* **86**, 563 (2014).
- [13] J. A. M. Paddison, M. Daum, Z. Dun, G. Ehlers, Y. Liu, M. B. Stone, H. Zhou, and M. Mourigal, Continuous excitations of the triangular-lattice quantum spin liquid YbMgGaO_4 , *Nat. Phys.* **13**, 117 (2017).
- [14] N. Li, Q. Huang, X. Y. Yue, W. J. Chu, Q. Chen, E. S. Choi, X. Zhao, H. D. Zhou, and X. F. Sun, Possible itinerant excitations and quantum spin state transitions in the effective spin-1/2 triangular-lattice antiferromagnet $\text{Na}_2\text{BaCo}(\text{PO}_4)_2$, *Nat. Commun.* **11**, 4216 (2020).
- [15] J. G. Cheng, G. Li, L. Balicas, J. S. Zhou, J. B. Goodenough, C. Xu, and H. D. Zhou, High-pressure sequence of $\text{Ba}_3\text{NiSb}_2\text{O}_9$ structural phases: New $S = 1$ quantum spin liquids based on Ni^{2+} , *Phys. Rev. Lett.* **107**, 197204 (2011).
- [16] H. D. Zhou, C. Xu, A. M. Hallas, H. J. Silverstein, C. R. Wiebe, I. Umegaki, J. Q. Yan, T. P. Murphy, J.-H. Park, Y. Qiu, J. R. D. Copley, J. S. Gardner, and Y. Takano, Successive phase transitions and extended spin-excitation continuum in the $S = 1/2$ triangular-lattice antiferromagnet $\text{Ba}_3\text{CoSb}_2\text{O}_9$, *Phys. Rev. Lett.* **109**, 267206 (2012).
- [17] Y. Gao, Y.-C. Fan, H. Li, F. Yang, X.-T. Zeng, X.-L. Sheng, R. Zhong, Y. Qi, Y. Wan, and W. Li, Spin supersolidity in nearly ideal easy-axis triangular quantum antiferromagnet $\text{Na}_2\text{BaCo}(\text{PO}_4)_2$, *npj Quantum Mater.* **7**, 89 (2022).
- [18] J. Sheng, J.-W. Mei, L. Wang, X. Xu, W. Jiang, L. Xu, H. Ge, N. Zhao, T. Li, A. Candini, B. Xi, J. Zhao, Y. Fu, J. Yang, Y. Zhang, G. Biasiol, S. Wang, J. Zhu, P. Miao, X. Tong, D. Yu, R. Mole, Y. Cui, L. Ma, Z. Zhang, Z. Ouyang, W. Tong, A. Podlesnyak, L. Wang, F. Ye, D. Yu, W. Yu, L. Wu, and Z. Wang, Bose-Einstein condensation of a two-magnon bound state in a spin-1 triangular lattice, *Nat. Mater.* **24**, 544 (2025).
- [19] M. M. Bordelon, E. Kenney, C. Liu, T. Hogan, L. Posthuma, M. Kavand, Y. Lyu, M. Sherwin, N. P. Butch, C. Brown, M. J. Graf, L. Balents, and S. D. Wilson, Field-tunable quantum disordered ground state in the triangular-lattice antiferromagnet NaYbO_2 , *Nat. Phys.* **15**, 1058 (2019).
- [20] J. Xiang, C. Zhang, Y. Gao, W. Schmidt, K. Schmalzl, C.-W. Wang, B. Li, N. Xi, X.-Y. Liu, H. Jin, G. Li, J. Shen, Z. Chen, Y. Qi, Y. Wan, W. Jin, W. Li, P. Sun, and G. Su, Giant magnetocaloric effect in spin supersolid candidate $\text{Na}_2\text{BaCo}(\text{PO}_4)_2$, *Nature* **625**, 270 (2024).
- [21] Z.-F. Ding, Y.-X. Yang, J. Zhang, C. Tan, Z.-H. Zhu, G. Chen, and L. Shu, Possible gapless spin liquid in the rare-earth kagome lattice magnet $\text{Tm}_3\text{Sb}_3\text{Zn}_2\text{O}_{14}$, *Phys. Rev. B* **98**, 174404 (2018).
- [22] B. Fåk, E. Kermarrec, L. Messio, B. Bernu, C. Lhuillier, F. Bert, P. Mendels, B. Koteswararao, F. Bouquet, J. Ollivier, A. D. Hillier, A. Amato, R. H. Colman, and A. S. Wills, Kapellasite: A kagome quantum spin liquid with competing interactions, *Phys. Rev. Lett.* **109**, 037208 (2012).
- [23] J. S. Helton, K. Matan, M. P. Shores, E. A. Nytko, B. M. Bartlett, Y. Yoshida, Y. Takano, A. Suslov, Y. Qiu, J.-H. Chung, D. G. Nocera, and Y. S. Lee, Spin dynamics of the spin-1/2 kagome lattice antiferromagnet $\text{ZnCu}_3(\text{OH})_6\text{Cl}_2$, *Phys. Rev. Lett.* **98**, 107204 (2007).
- [24] Y. Singh, S. Manni, J. Reuther, T. Berlijn, R. Thomale, W. Ku, S. Trebst, and P. Gegenwart, Relevance of the Heisenberg-Kitaev model for the honeycomb lattice iridates A_2IrO_3 , *Phys. Rev. Lett.* **108**, 127203 (2012).
- [25] Y. Matsumoto, S. Schnierer, J. A. N. Bruin, J. Nuss, P. Reiss, G. Jackeli, K. Kitagawa, and H. Takagi, A quantum critical Bose gas of magnons in the quasi-two-dimensional antiferromagnet YbCl_3 under magnetic fields, *Nat. Phys.* **20**, 1131 (2024).
- [26] Y. Kojima, M. Watanabe, N. Kurita, H. Tanaka, A. Matsuo, K. Kindo, and M. Avdeev, Quantum magnetic properties of the spin-1/2 triangular-lattice antiferromagnet $\text{Ba}_2\text{La}_2\text{CoTe}_2\text{O}_{12}$, *Phys. Rev. B* **98**, 174406 (2018).
- [27] B. C. Yu, J. Y. Yang, D. J. Gawryluk, Y. Xu, Q. F. Zhan, T. Shiroka, and T. Shang, Neutron scattering and muon-spin spectroscopy studies of the magnetic triangular-lattice compounds $\text{A}_2\text{La}_2\text{NiW}_2\text{O}_{12}$ ($A = \text{Sr}, \text{Ba}$), *Phys. Rev. Mater.* **7**, 074403 (2023).
- [28] M. Saito, M. Watanabe, N. Kurita, A. Matsuo, K. Kindo, M. Avdeev, H. O. Jeschke, and H. Tanaka, Successive phase transitions and magnetization plateau in the spin-1 triangular-

- lattice antiferromagnet $\text{Ba}_2\text{La}_2\text{NiTe}_2\text{O}_{12}$ with small easy-axis anisotropy, *Phys. Rev. B* **100**, 064417 (2019).
- [29] R. Rawl, M. Lee, E. S. Choi, G. Li, K. W. Chen, R. Baumbach, C. R. Dela Cruz, J. Ma, and H. D. Zhou, Magnetic properties of the triangular lattice magnets $A_4B'B_2O_{12}$ ($A = \text{Ba}, \text{Sr}, \text{La}$; $B' = \text{Co}, \text{Ni}, \text{Mn}$; $B = \text{W}, \text{Re}$), *Phys. Rev. B* **95**, 174438 (2017).
- [30] Y. Doi, M. Wakeshima, K. Tezuka, Y. J. Shan, K. Ohoyama, S. Lee, S. Torii, T. Kamiyama, and Y. Hinatsu, Crystal structures, magnetic properties, and DFT calculation of B -site defected 12L-perovskites $\text{Ba}_2\text{La}_2\text{MW}_2\text{O}_{12}$ ($M = \text{Mn}, \text{Co}, \text{Ni}, \text{Zn}$), *J. Phys.: Condens. Matter* **29**, 365802 (2017).
- [31] P. Park, E. A. Ghioldi, A. F. May, J. A. Kolopus, A. A. Podlesnyak, S. Calder, J. A. M. Paddison, A. E. Trumper, L. O. Manuel, C. D. Batista, M. B. Stone, G. B. Halász, and A. D. Christianson, Anomalous continuum scattering and higher-order van Hove singularity in the strongly anisotropic $S = 1/2$ triangular lattice antiferromagnet, *Nat. Commun.* **15**, 7264 (2024).
- [32] For details on the material synthesis, magnetic susceptibility, heat capacity, wTF- and LF- μ SR spectra, neutron powder diffraction, theoretical simulations, as well as for the data analysis, see the Supplementary Material at <http://link.aps.org/supplemental/XXX/PhysRevlett.XXX>.
- [33] Q. Li, H. Li, J. Zhao, H.-G. Luo, and Z. Y. Xie, Magnetization of the spin- $1/2$ Heisenberg antiferromagnet on the triangular lattice, *Phys. Rev. B* **105**, 184418 (2022).
- [34] T. Nishino and K. Okunishi, Corner transfer matrix renormalization group method, *J. Phys. Soc. Jpn.* **65**, 891 (1996).
- [35] P. Corboz, J. Jordan, and G. Vidal, Simulation of fermionic lattice models in two dimensions with projected entangled-pair states: Next-nearest neighbor Hamiltonians, *Phys. Rev. B* **82**, 245119 (2010).
- [36] Z. Tian, C. Zhu, Z. Ouyang, J. Wang, W. Tong, Y. Liu, Z. Xia, and S. Yuan, Susceptibility, high-field magnetization and ESR studies in a spin-5/2 triangular-lattice antiferromagnet $\text{Ba}_3\text{MnSb}_2\text{O}_9$, *J. Magn. Magn. Mater.* **360**, 10 (2014).
- [37] Z. Y. Xie, J. Chen, J. F. Yu, X. Kong, B. Normand, and T. Xiang, Tensor renormalization of quantum many-body systems using projected entangled simplex states, *Phys. Rev. X* **4**, 011025 (2014).
- [38] P. Fischer, G. Frey, M. Koch, M. Könnecke, V. Pomjakushin, J. Schefer, R. Thut, N. Schlumpf, R. Bürge, U. Greuter, S. Bondt, and E. Berruyer, High-resolution powder diffractometer HRPT for thermal neutrons at SINQ, *Phys. B: Condens. Matter* **276-278**, 146 (2000).
- [39] A. Suter and B. M. Wojek, Musrfit: A free platform-independent framework for μ SR data analysis, *Phys. Procedia* **30**, 69 (2012).
- [40] X. Y. Zhu, H. Zhang, D. J. Gawryluk, Z. X. Zhen, B. C. Yu, S. L. Ju, W. Xie, D. M. Jiang, W. J. Cheng, Y. Xu, M. Shi, E. Pomjakushina, Q. F. Zhan, T. Shiroka, and T. Shang, Spin order and fluctuations in the EuAl_4 and EuGa_4 topological antiferromagnets: A μ SR study, *Phys. Rev. B* **105**, 014423 (2022).
- [41] Y. Wang, Z. Zhen, J. Meng, I. Plokhikh, D. Wu, D. J. Gawryluk, Y. Xu, Q. Zhan, M. Shi, E. Pomjakushina, T. Shiroka, and T. Shang, Spin order and dynamics in the topological rare-earth germanide semimetals, *Sci. China Phys., Mech. Astron.* **67**, 107512 (2024).
- [42] A. Fennell, V. Y. Pomjakushin, A. Uldry, B. Delley, B. Prévost, A. Désilets-Benoit, A. D. Bianchi, R. I. Bewley, B. R. Hansen, T. Klimczuk, R. J. Cava, and M. Kenzelmann, Evidence for SrHo_2O_4 and SrDy_2O_4 as model J_1 - J_2 zigzag chain materials, *Phys. Rev. B* **89**, 224511 (2014).
- [43] P. H. Conlon and J. T. Chalker, Absent pinch points and emergent clusters: Further neighbor interactions in the pyrochlore Heisenberg antiferromagnet, *Phys. Rev. B* **81**, 224413 (2010).
- [44] L. Ding, F. Orlandi, D. Khalyavin, A. Boothroyd, D. Prabhakaran, G. Balakrishnan, and P. Manuel, Coupling between spin and charge order driven by magnetic field in triangular Ising system $\text{LuFe}_2\text{O}_{4+\delta}$, *Crystals* **8**, 88 (2018).
- [45] J. Xing, L. D. Sanjeeva, J. Kim, G. R. Stewart, A. Podlesnyak, and A. S. Sefat, Field-induced magnetic transition and spin fluctuations in the quantum spin-liquid candidate CsYbSe_2 , *Phys. Rev. B* **100**, 220407 (2019).
- [46] Y. Kojima, N. Kurita, H. Tanaka, and K. Nakajima, Magnons and spinons in $\text{Ba}_2\text{CoTeO}_6$: A composite system of isolated spin- $1/2$ triangular Heisenberg-like and frustrated honeycomb Ising-like antiferromagnets, *Phys. Rev. B* **105**, L020408 (2022).
- [47] K. Fritsch, K. A. Ross, G. E. Granroth, G. Ehlers, H. M. L. Noad, H. A. Dabkowska, and B. D. Gaulin, Quasi-two-dimensional spin correlations in the triangular lattice bilayer spin glass LuCoGaO_4 , *Phys. Rev. B* **96**, 094414 (2017).
- [48] P. Anderson, Resonating valence bonds: A new kind of insulator?, *Mater. Res. Bull.* **8**, 153 (1973).
- [49] M. F. Collins and O. A. Petrenko, Triangular antiferromagnets, *Can. J. Phys.* **75**, 605 (1997).
- [50] Y. Shirata, H. Tanaka, A. Matsuo, and K. Kindo, Experimental realization of a spin-1/2 triangular-lattice Heisenberg antiferromagnet, *Phys. Rev. Lett.* **108**, 057205 (2012).
- [51] O. A. Starykh, Unusual ordered phases of highly frustrated magnets: A review, *Rep. Prog. Phys.* **78**, 052502 (2015).
- [52] J. Alicea, A. V. Chubukov, and O. A. Starykh, Quantum stabilization of the 1/3-magnetization plateau in Cs_2CuBr_4 , *Phys. Rev. Lett.* **102**, 137201 (2009).
- [53] M. Shu, W. Dong, J. Jiao, J. Wu, G. Lin, Y. Kamiya, T. Hong, H. Cao, M. Matsuda, W. Tian, S. Chi, G. Ehlers, Z. Ouyang, H. Chen, Y. Zou, Z. Qu, Q. Huang, H. Zhou, and J. Ma, Static and dynamical properties of the spin-5/2 nearly ideal triangular lattice antiferromagnet $\text{Ba}_3\text{MnSb}_2\text{O}_9$, *Phys. Rev. B* **108**, 174424 (2023).
- [54] M. Fujihala, X. G. Zheng, S. Lee, T. Kamiyama, A. Matsuo, K. Kindo, and T. Kawae, Spin order in the Heisenberg kagome antiferromagnet $\text{MgFe}_3(\text{OH})_6\text{Cl}_2$, *Phys. Rev. B* **96**, 144111 (2017).
- [55] Y.-X. Yang, C.-Y. Jiang, L.-L. Huang, Z.-H. Zhu, C.-S. Chen, Q. Wu, Z.-F. Ding, C. Tan, K.-W. Chen, P. K. Biswas, A. D. Hillier, Y.-G. Shi, C. Liu, L. Wang, F. Ye, J.-W. Mei, and L. Shu, Muon spin relaxation study of spin dynamics on a Kitaev honeycomb material $\text{H}_3\text{LiIr}_2\text{O}_6$, *npj Quantum Mater.* **9**, 1 (2024).
- [56] J. A. Sears, M. Songvilay, K. W. Plumb, J. P. Clancy, Y. Qiu, Y. Zhao, D. Parshall, and Y.-J. Kim, Magnetic order in α - RuCl_3 : A honeycomb-lattice quantum magnet with strong spin-orbit coupling, *Phys. Rev. B* **91**, 144420 (2015).
- [57] F. Lang, P. J. Baker, A. A. Haghighirad, Y. Li, D. Prabhakaran, R. Valentí, and S. J. Blundell, Unconventional magnetism on a honeycomb lattice in α - RuCl_3 studied by muon spin rotation, *Phys. Rev. B* **94**, 020407 (2016).
- [58] Y. Li, D. Adroja, P. K. Biswas, P. J. Baker, Q. Zhang, J. Liu, A. A. Tsirlin, P. Gegenwart, and Q. Zhang, Muon spin relaxation evidence for the $U(1)$ quantum spin-liquid ground state in the triangular antiferromagnet YbMgGaO_4 , *Phys. Rev. Lett.* **117**, 097201 (2016).
- [59] L. Ding, P. Manuel, S. Bachus, F. Größler, P. Gegenwart, J. Singleton, R. D. Johnson, H. C. Walker, D. T. Adroja, A. D. Hillier, and A. A. Tsirlin, Gapless spin-liquid state in the structurally disorder-free triangular antiferromagnet NaYbO_2 , *Phys. Rev. B* **100**, 144432 (2019).
- [60] A. V. Chubukov and D. I. Golosov, Quantum theory of an antiferromagnet on a triangular lattice in a magnetic field, *J. Phys.: Condens. Matter* **3**, 69 (1991).
- [61] M. Ye and A. V. Chubukov, Quantum phase transitions in the Heisenberg J_1 - J_2 triangular antiferromagnet in a magnetic field, *Phys. Rev. B* **95** (2017).
- [62] A. V. Chubukov and T. Jolicoeur, Order-from-disorder phenomena in Heisenberg antiferromagnets on a triangular lattice, *Phys. Rev. B* **46**, 11137 (1992).
- [63] H. Nakano and T. Sakai, Magnetization process of the spin-1/2 triangular-lattice Heisenberg antiferromagnet with next-nearest-neighbor interactions - plateau or nonplateau, *J. Phys.*

